Solar Energy 236 (2022) 782–789

Contents lists available at ScienceDirect

Solar Energy

journal homepage: www.elsevier.com/locate/solener

Atmospheric attenuation measurement system for commercial solar plants based on optical spectrum analysis

Carlos Heras [a,*], Iñigo Salinas [a], Marina Sevilla [c], Rocio Chueca [a], Sonia Escorza [b], Carlos Fernández–Peruchena [b], Ana Bernardos [b], Pascual Sevillano [a], Marcelino Sánchez [b]

[a] Aragon Institute of Engineering Research (I3A), Universidad de Zaragoza, C/Mariano Esquillor, 50018 Zaragoza, Spain
[b] National Renewable Energy Centre (CENER), C/ Ciudad de la Innovación 7, 31621 Sarriguren, Spain
[c] Aragon Photonics Labs, C/ Prado 5, 50009 Zaragoza, Spain

ARTICLE INFO

Keywords:
Atmospheric attenuation measurement
central receiver CSP
VIS-IR optical spectrum measurement
Global solar energy measurement
Atmospheric attenuation modeling
Solar tower plants

ABSTRACT

The measurement of the solar radiation attenuation is one of the main challenges in concentrating solar power technologies. This work presents a new strategy for this measurement, based on the analysis of the VIS and IR spectra, and its related system. The optical design of the system and its implementation in a central receiver solar power plant is described, and the experimental results are detailed. We present, to the best of our knowledge, the first measurements of the atmospheric attenuation spectrum in a solar power plant. This system provides direct measurements of real atmospheric attenuation values, which opens the way to analyze the impact of aerosols and meteorological conditions at surface level in this attenuation.

1. Introduction

There are many parameters that directly impact the electrical power generation efficiency of central receiver concentrating solar power (CR-CSP) plants (Fernández-Peruchena et al., 2018). The attenuation of the atmosphere at the solar plant level is one of them, and is still an open field of study. The atmospheric attenuation of solar rays reflected by the collector elements on their path towards the receiver element is due to the phenomena of scattering (or diffusion) and absorption of light when it travels through the atmosphere at the terrestrial level. Both the scattering and the energy absorption phenomenon are due to interaction with aerosol particles suspended in the atmosphere, as well as gases dissolved therein (Polo et al., 2016). This attenuation is a function of the type and number of air molecules and particles in the path of the solar rays.

Different approaches to infer the value of the atmospheric attenuation in solar plants have been tested (Hanrieder et al., 2017). Most of them use measurements combined with atmospheric and radiative models to estimate the attenuation (Ali Rahoma and Hassan, 2012; Hanrieder et al., 2016; Shaw et al., 1973; Wen and Yeh, 2010). Other published techniques are based on the measurement of the light power difference between different locations of the plant, for example by using pyrheliometers measuring direct radiation from the sun and reflected by the heliostats at different positions (Tahboub et al., 2012), or by using digital cameras taking simultaneous photographs of a screen at different distances (Ballestrín et al., 2019, 2018). These setups rely on direct measurements, but they can also show major uncertainties. In the case of pyrheliometers, due to their precision and the uncertainty in the geometry of the heliostat and the ray tracing employed. In the case of digital cameras, CCD sensors integrate all the visible spectrum and report a single averaged value, but the IR range is not considered and the solar weighted attenuation (average attenuation calculated from the attenuation at each wavelength and weighted using a standard solar spectrum) cannot be calculated.

In this paper, we present a new measurement strategy - and its related system - to measure the atmospheric attenuation in solar plants. It is based on the measurement of VIS and IR spectra of the sun radiation reflected by a white diffuser screen at two suitable locations of the plant. The system uses optical telescopes to collect enough radiation for high wavelength resolution and intensity accuracy over the measured spectrum. Since the VIS and IR spectra are measured, the system reports both the atmospheric attenuation at each wavelength in the solar optical

* Corresponding author.
E-mail addresses: cdheras@unizar.es (C. Heras), isalinas@unizar.es (I. Salinas), m.sevilla@aragonphotonics.com (M. Sevilla), rchueca@unizar.es (R. Chueca), sescorza@cener.com (S. Escorza), cfernandez@cener.com (C. Fernández–Peruchena), abernardos@cener.com (A. Bernardos), psevi@unizar.es (P. Sevillano), msanchez@cener.com (M. Sánchez).

https://doi.org/10.1016/j.solener.2022.03.057
Received 18 June 2021; Received in revised form 27 January 2022; Accepted 21 March 2022
Available online 28 March 2022

range and the solar-weighted attenuation of the plant. This is achieved without inaccuracies due to wavelength dependencies of the contributions to the measurement (Ineichen, 2008; Molineaux and Ineichen, 1996), such as the different atmospheric attenuation sources or the diffused light background existing in the plant.

Moreover, the data obtained allows us to analyze the different origins of atmospheric attenuation, as the resolution in wavelength is enough to resolve absorption bands of different compounds, such as water, and the subtler wavelength dependency of the attenuation due to suspended particles for different weather conditions. From this analysis, an accurate model to calculate the atmospheric attenuation for any heliostat of the plant can be implemented (Marzo et al., 2021; Mishra et al., 2020), and hence the global solar energy reaching the receptor can be predicted (Ballestrín and Marzo, 2012).

The system has been set up and tested at PS10, a commercial solar thermal power plant, with central receiver system at Sanlúcar la Mayor (Seville, Spain) owned by Atlantica Sustainable Infrastructure Plc (Solnova Solar Power Plant). In this paper, we present the first results obtained as a test of its performance. To the best of our knowledge, this is the first time that a solar-weighted attenuation for an operating commercial solar plant, calculated from the atmospheric attenuation at each wavelength in the solar optical range, is reported in the literature.

2. System descripction

The system is based on a white diffuser screen that reflects the radiation from the sun and two optical devices to measure the spectrum of that reflected radiation. One of the devices (Near) is located at a short distance from the screen to obtain a reference measurement. The other one (Far) is located at a larger distance (ideally around 1 km). The ratio between the spectra measured by the two devices provides the attenuation spectrum of the atmosphere in the distance between the two locations. The light background level for both devices is accounted for in a measurement using a black screen.

The system has been installed in the PS10 CR-CSP plant, and its basic diagram is shown in Fig. 1. Both diffuser screens are located at the end of the plant and south oriented, just behind the last line of heliostats. The reference or Near device is located at a 50 m distance from it, whereas the other is located at middle height level (31 m) at the Atlantica solar tower, both north oriented and protected from weather conditions. The devices have 4G data connection for real time control and data report. The main control unit is integrated in the device placed at the tower and can also be connected to a remote PC for control or measurement analysis. Measurements can be taken every 120 s. Some images of the different elements of the system at the solar plant are shown in Fig. 2.

The dimensions of the diffuser screen, Fig. 2.(A) should be large enough to fill the field of view of the devices, 2 m × 2 m in our setup. All the elements are properly fixed to the ground to resist extreme weather conditions and the area is signposted for security.

The devices, Fig. 2(B) and (C), comprise three main parts as depicted in Fig. 3: capture optics, detection module and control module. The capture optics include a telescope, an eyepiece and a diaphragm. The telescope is based on a Cassegrain reflector design (Optics, 2000), and it provides a large capture area in the optics, which assures that enough radiation intensity is available in the system to accurately measure the spectrum in the detection module.

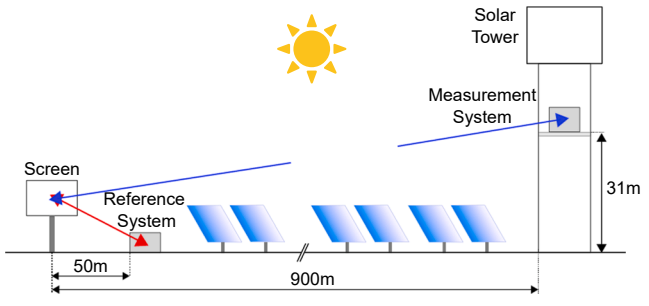

Fig. 1. Basic diagram of the system installed in the operating solar plant.

The field of view, limited by both the focal length of the telescope and the diaphragm, is 2 mrad for the Far device and 6 mrad for the Near device. These values are adjusted to ensure that the white/black screen fills the field of view of the system, including possible deviations of the beams outside and inside the equipment over long periods of time due to changes in air refraction caused by temperature, expansion and compression of mechanical components or vibration effects among others. Since it is a very important feature of the system, a visual control in real time is required. This control is included in the detection module by a CCD camera as described below. After the diaphragm, the eyepiece collimates the radiation captured by the telescope optics and directs it to the detection module. Note, as discussed later, that the optics not only captures the radiation reflected from the screen, but also the background diffuse light in the beam path.

The detection module comprises two wavelength independent beam splitters. The first one has a 10/90 splitting ratio, to direct a small fraction of the captured radiation to a CCD camera. This camera includes a basic optical system focused on the diaphragm for real time control of the alignment of the device to the screen. The remaining 90% power is used in the measurement. A second 50/50 beam splitter directs the light to the two array spectrometers, one in the VIS range and the other in the near IR range. The two spectrometers and the camera are controlled via USB by the control module.

Array spectrometers suffer from two well-known drawbacks: temperature dependence and nonlinear response to radiation intensity (Brady, 2008). The electrical currents generated by the array sensors change with temperature, resulting in uncertainty in the measured signal. Parameters like baseline drift, dark current, dark noise and responsivity among others are very sensitive to temperature (D'Amato et al., 2007). Although their values should be stable for each temperature and can be calibrated, we have found preferable to include a cooling stage to maintain the four spectrometers at a constant temperature of 27 °C and so avoid any temperature dependence. The background levels of the electrical currents generated by each spectrometer in the condition of no incident radiation at 27 °C are measured and later discounted.

The second problem is that the reported counts per second are not linear with the integration time (Smith, 2007). When high accuracy measurements are required, it is necessary to correct this nonlinearity. Thus, a linearity calibration process was performed in the laboratory by measuring the response of each pixel to a constant light source while integration times were changed, at a working temperature of 27 °C. The obtained data was stored in a 3D linearity matrix (wavelength, integration time and counts) which is used to correct and linearize future measurements.

Having all of these considerations in mind, uncertainties in the attenuation at each wavelength lower than absolute 1% can be achieved for different sunlight intensity levels and longtime intervals. The wavelength range of the system is 400–1630 nm with a resolution of 5 nm below 900 nm and 10 nm over 900 nm. No temperature dependence has been observed in the 10–45 °C range.

Before its installation, the system was calibrated. The Near and Far devices are placed at the same short distance from the white screen, so that the same radiation intensity at each wavelength reaches both of them. The ratio of their measured spectra at each wavelength, $K(\lambda)$, determines the calibration ratio of their relative measured signals. Note that the intensity measured by the Far device will not vary with the distance to the screen as long as that screen fills its field of view, so the calibration ratio $K(\lambda)$ remains valid when this device is installed in its final location in the tower. Once the system was installed, the value of the ratio $K(\lambda)$ between the intensity values measured by each device was checked each month using a white screen placed before them, reporting variations under 0.5%.

Fig. 2. Images of the elements at the PS10 solar tower power plant. (A) White diffuser screen. (B) Far measurement device placed in the tower. (C) Near measurement device located at ground level.

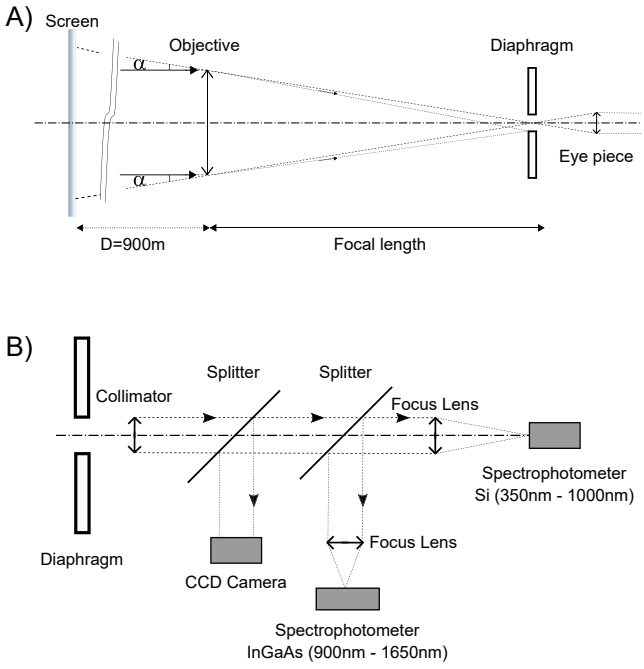

Fig. 3. Schematic of the telescope optics (A), and the detection module (B).

Once the system has been calibrated, the measurement process is simple. Both devices are placed at their corresponding distances and pointed to the white screen, and their measured spectra, $S^{w}_{Far}(\lambda)$ and $S^{w}_{Near}(\lambda)$, are acquired. After that, the devices are pointed to the black screen and the difference between their measured spectra, $S^{b}_{Far}(\lambda)$ and, $S^{b}_{Near}(\lambda)$, determines the background radiation during the measurement. The main source of this background is the diffuse light present in the plant. Finally, the atmospheric attenuation for the slant path at each wavelength $At_s(\lambda)$ and the solar-weighted atmospheric attenuation At_s are obtained from the following expressions:

$$At_s(\lambda) = 1 - \frac{S^{w}_{Far}(\lambda) - \left(S^{b}_{Far}(\lambda) - S^{b}_{Near}(\lambda)\right)}{S^{w}_{Near}(\lambda)} \bullet \mathrm{K}(\lambda) = 1 - \mathrm{T_s}(\lambda) \tag{1}$$

$$At_s = 1 - \int_{\lambda_0}^{\lambda_f} T(\lambda) \bullet \mathrm{S_{sun}}(\lambda) \bullet \mathrm{d}\lambda \tag{2}$$

Where $T_s(\lambda)$ is the transmittance at each wavelength, $S_{sun}(\lambda)$ is the solar spectral power distribution according to ASTM G173–03 standard, λ_0 and λ_f are the limits of the considered wavelength range.

The main problem of the atmospheric attenuation measurement is that there is no standard to compare it to. Thus, it is not possible to evaluate the accuracy of an atmospheric attenuation measurement system, and when a global atmospheric attenuation value is reported, there is no mean to be sure what has been really measured or to evaluate the possible error in it. Our strategy is based on the analysis of the spectrum and provides some advantages when compared to other techniques reporting a single wavelength value or a broadband average.

First, the analysis of the measurements makes possible the assessment of the stability of the system. When comparing the normalized spectra measured by each device along consecutive days with similar atmospheric conditions, the differences are within the estimated uncertainty. This does not guarantee the accuracy of the global atmospheric attenuation value, but it shows that the measurements are not affected by any variance not attributable to atmospheric changes.

Second, since $At_s(\lambda)$ is measured at each wavelength, we can determine that there are no errors due to wavelength dependency or spectral variations of the different factors that are involved in the measurement, like sensor responsivity, screen reflectance or the diffuse light background.

Third, the spectral analysis of the atmospheric attenuation allows us to identify the presence and evaluate the magnitude of the different possible causes of attenuation, such as absorbing molecules or scattering particles.

And fourth, the determination of these magnitudes opens the way to generate accurate models to calculate the atmospheric attenuation of the radiation reflected by any heliostat of the solar plant, without inaccuracies due to dependence of the spectral attenuation with the heliostat-tower distance.

3. Results

The results presented below were obtained at a commercial solar plant along the winter of 2020–2021, a limiting season from a measurement point of view due to low DNI values.

As an example, we show first in Fig. 4 the visible and IR spectra at different hours along the same day, for both the Near and Far devices (10:00 h, 11:00 h, 13:00 h, 15:00 h, and 16:30 h UMT + 1 on December 27, 2020). The evolution of the measured solar radiation intensity along the day can be easily observed at each location, in accord with DNI variations. In these measurements the background signal at the spectrometer has been subtracted and the linearity matrix applied. The measurement interval is 5 nm in the VIS and 10 nm in the IR.

Integration times - indicated for each curve - vary from 52 ms to 285 ms in the visible range, depending on the available light intensity, while they remain always at 4 s for the infrared. The saturation level of the spectrometers is around 60.000 counts, but nonlinearity rises sharply

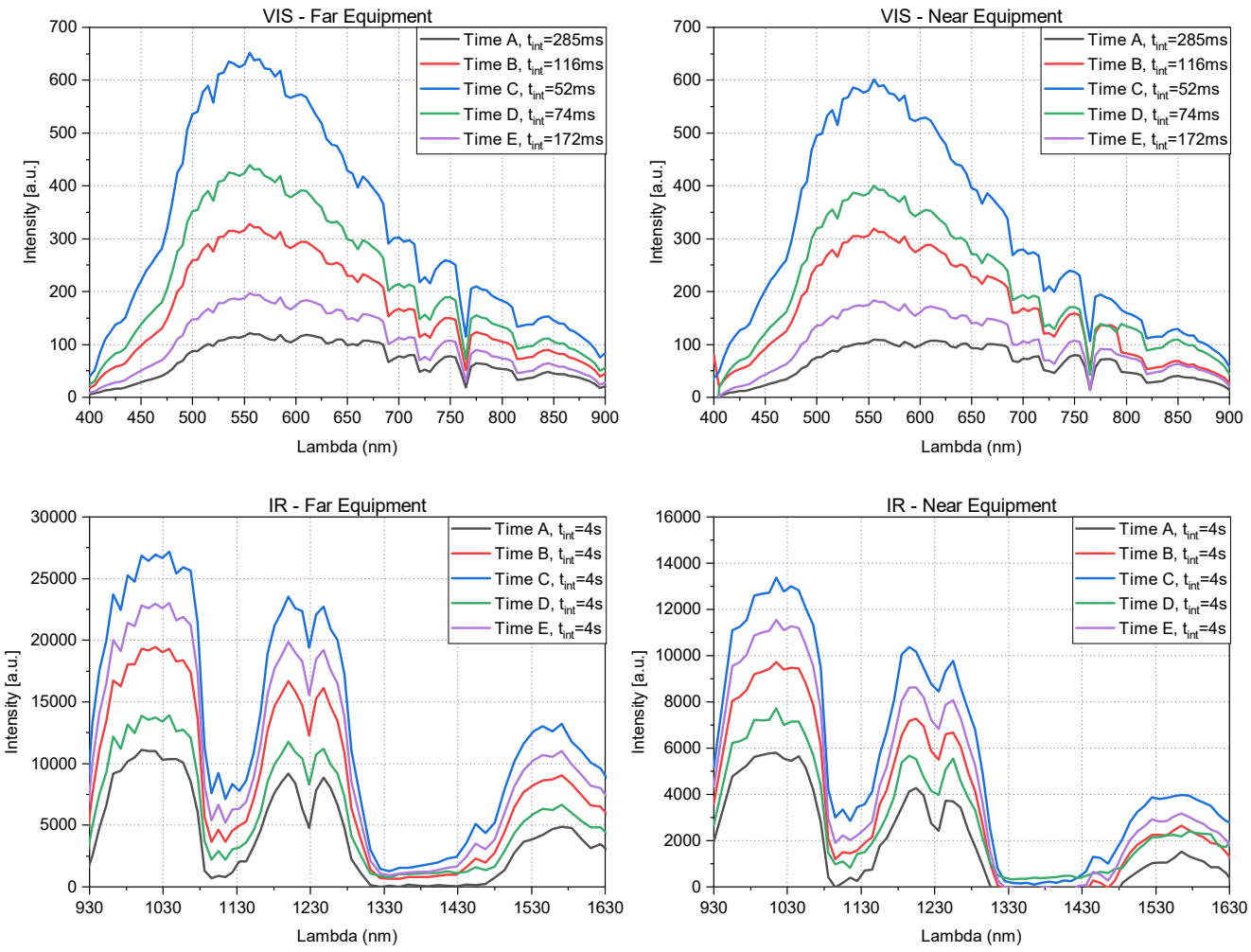

Fig. 4. VIS and IR measured spectra at different hours of the same day for the Far and Near equipment. Time A-E series correspond to measurements and its integration time recorded on December 27 at 10:00 h, 11:00 h, 13:00 h, 15:00 h, and 16:30 h UMT + 1 respectively.

above 50.000 counts. Therefore, we limit the integration time to obtain a maximum value of 40.000 counts in the overall spectral range, so that our measurements remain in the most linear range of the devices and, by applying our previous calibration, we are able to achieve a stability better than 0.5% in the measured intensity at each wavelength.

In the setup under evaluation and for simplicity, the measurement uses the same integration time for every acquisition. This results in low signal levels at the 875 nm-950 nm and 1300 nm-1400 nm wavelength ranges where the water absorption peaks are also present. However, this could be easily solved, if necessary, for example using larger integration times for these ranges in the case of high precision molecular absorption peak studies.

These intensity curves represent measured counts divided by integration time, and their data corresponds to the $S^{w}_{Far}(\lambda)$ and $S^{w}_{Near}(\lambda)$, values in Eq. (1). Note that, although these values are affected by the spectral responsivity of the array sensors, the high dependence of the responsivity with the wavelength has no impact on the calculations since it is directly cancelled in Eq. (1).

For a better comparison and analysis of these spectra, we show in Fig. 5 the curves normalized to their maximum values, which clearly shows their evolution along the day. On one hand, for each device, we can observe the variation due to the changes in the spectral solar irradiance with the sun elevation. The differences in the air mass traversed by the radiation from the sun produce, for example, a well-known increase of the red-to-blue ratio in the irradiance spectrum when the sun is near the horizon.

On the other hand, when comparing the evolution of the spectra between devices, these changes are different and wavelength dependent. As it is discussed later, there are mainly two contributions to these differences: the spectral variations of the DNI attenuation with the slant range along the day and the spectral variations of the diffuse light background which affects to the Far device measurement. Note that only this spectral measurement strategy provides the capacity to identify and analyze the magnitude of these contributions to the atmospheric attenuation measurement.

Prior to the analysis of these contributions, we will discuss the stability and accuracy of the system. In Fig. 6, we compare the normalized spectra measured at the same hour of different days with similar sun and weather conditions (November 19, 20 and 21, 2020). These curves show very high repeatability - better than 0,5% - for each point of the spectrum in the overall wavelength range for both devices.

This is only an approximation of the stability of the system, since there is not a controllable light source or atmospheric attenuation standard to evaluate exactly this measurement once the equipment has been installed. However, since we are comparing more than 200 points at different wavelengths for each measurement, it can be considered a good approximation. For example, this high stability allows us to observe small differences in the spectra at the water absorption peaks, as indicated in the charts. This is because, although solar and atmospheric aerosol conditions were similar along the three days, there were small variations in the air relative humidity (as indicated below) which are observable here.

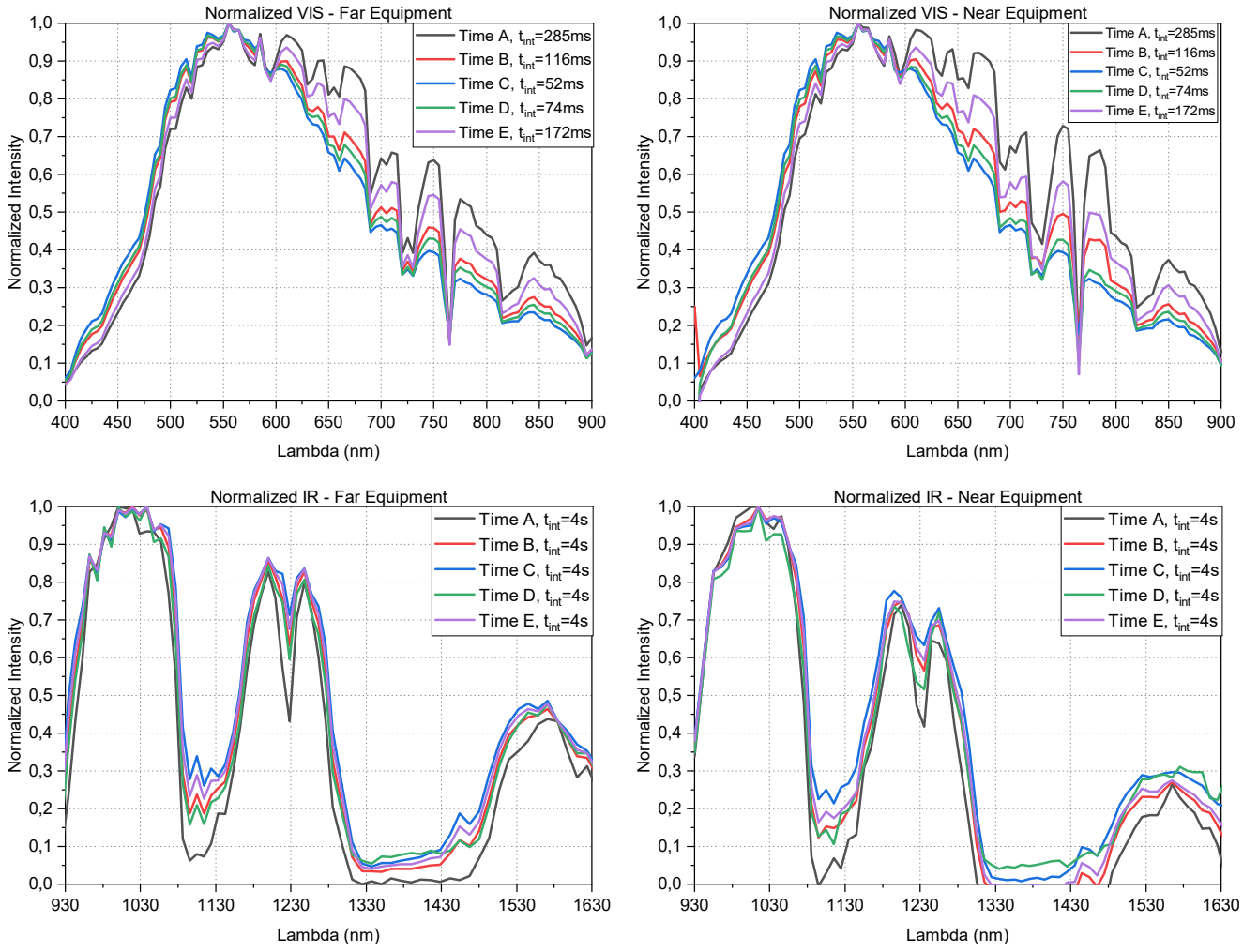

Fig. 5. Normalized VIS and IR spectra measured at different hours of the same day for the Far and Near equipment. Time A-E series correspond to measurements and its integration time recorded on December 27 at 10:00 h, 11:00 h, 13:00 h, 15:00 h, and 16:30 h UMT + 1 respectively.

The uncertainty of the atmospheric attenuation provided by the system is caused by the effect of the uncertainty in the measurements taken. By performing a propagation analysis on Eqs. (1) and (2) we can calculate its final value. Defining $M(\lambda)$ and its uncertainty, $\sigma_{M}(\lambda)$:

$$M(\lambda) = \frac{S^{w}_{Far}(\lambda) - \left(S^{b}_{Far}(\lambda) - S^{b}_{Near}(\lambda)\right)}{S^{w}_{Near}(\lambda)} \tag{3}$$

$$\sigma_{M(\lambda)} = \sqrt{\left(\frac{\sigma^{w}_{SF}(\lambda)}{S^{w}_{N}(\lambda)}\right)^{2} + \left(\frac{\sigma^{b}_{SF}(\lambda)}{S^{w}_{N}(\lambda)}\right)^{2} + \left(\frac{\sigma^{b}_{SN}(\lambda)}{S^{w}_{N}(\lambda)}\right)^{2} + \left(\frac{\sigma^{w}_{SN}(\lambda)\left[S^{w}_{F}(\lambda) - \left(S^{b}_{F}(\lambda) - S^{b}_{N}(\lambda)\right)\right]}{\left(S^{w}_{N}(\lambda)\right)^{2}}\right)^{2}} \tag{4}$$

The uncertainty associated to the single wavelength atmospheric attenuation, $\sigma_{AT}(\lambda)$, and for the solar weighted attenuation, σ_{At}, will be determined by:

$$\sigma_{At}(\lambda) = \sqrt{\left(\sigma_{M}(\lambda)\bullet K(\lambda)\right)^{2} + \left(\sigma_{K}(\lambda)\bullet M(\lambda)\right)^{2}} \tag{5}$$

$$\sigma_{At} = \sqrt{\int_{\lambda_0}^{\lambda_f} \left[\sigma_{At}(\lambda)\bullet S_{sun}(\lambda)\right]^{2} \bullet d\lambda} \tag{6}$$

Assuming similar values for the different $\sigma^{w,b}_{SF,N}(\lambda)$, as they are all measured using a similar procedure, and $\sigma^{w,b}_{SF,N}(\lambda)/S^{w,b}_{F,N}(\lambda) \leq 0.005$ (0.5%), this analysis shows that the uncertainty of the system for a single wavelength over time remains 1% in real working conditions at a solar plant, in consonance with the laboratory tests (Sánchez et al., 2019). Moreover, the global attenuation values may show much lower uncertainties depending on the wavelength selection.

Note that, as there is no standard to compare to, this 1% cannot be assumed as the accuracy of the absolute global atmospheric attenuation values.

To calculate the atmospheric attenuation, it is necessary to consider the background radiation and subtract its impact on the measured spectra as indicated in Eq. (1). The background radiation is measured by

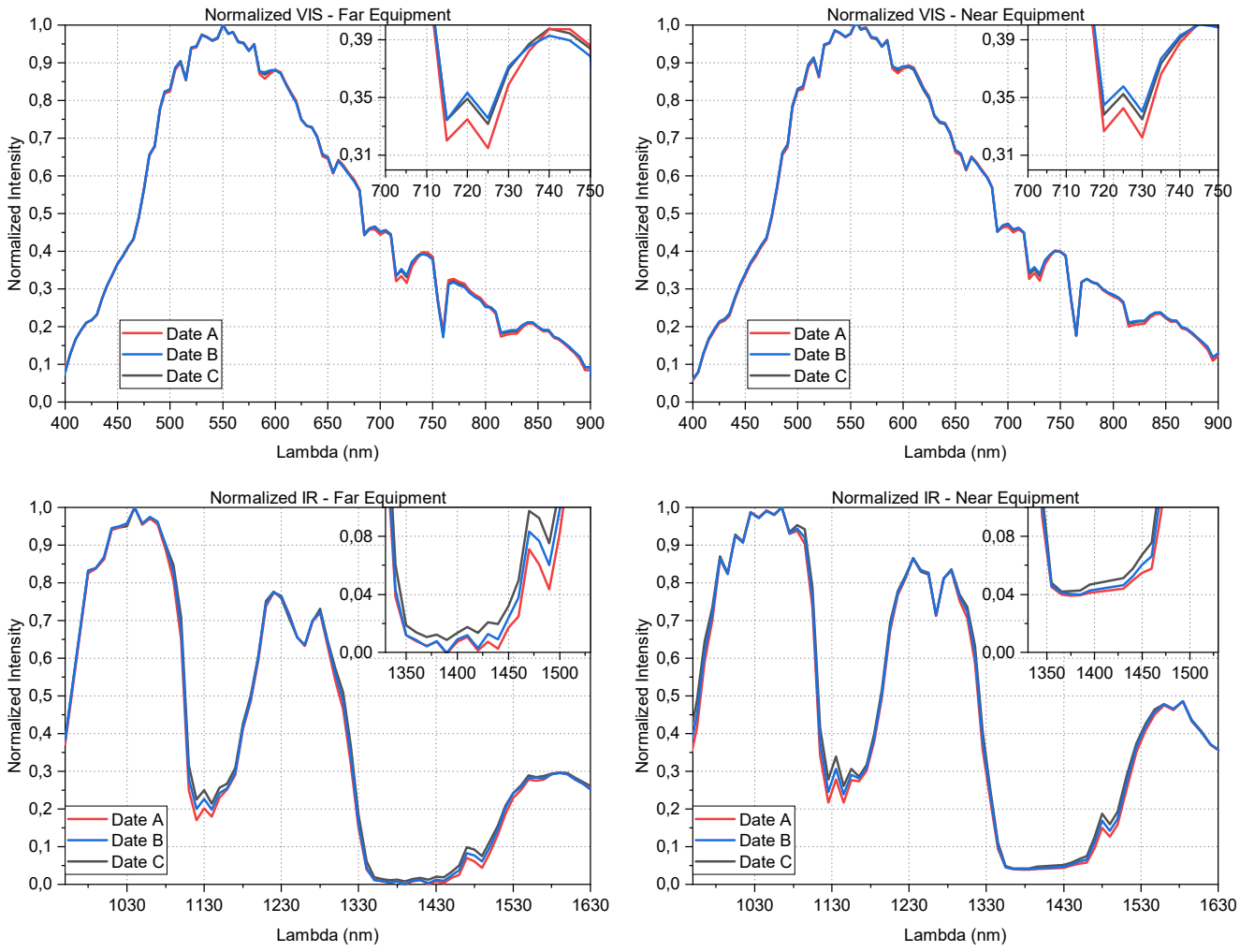

Fig. 6. Normalized VIS and IR spectra at the same hour of different days for the Far and Near equipment. Date A-C corresponds to measurements recorded on November 19, 20 and 21 respectively.

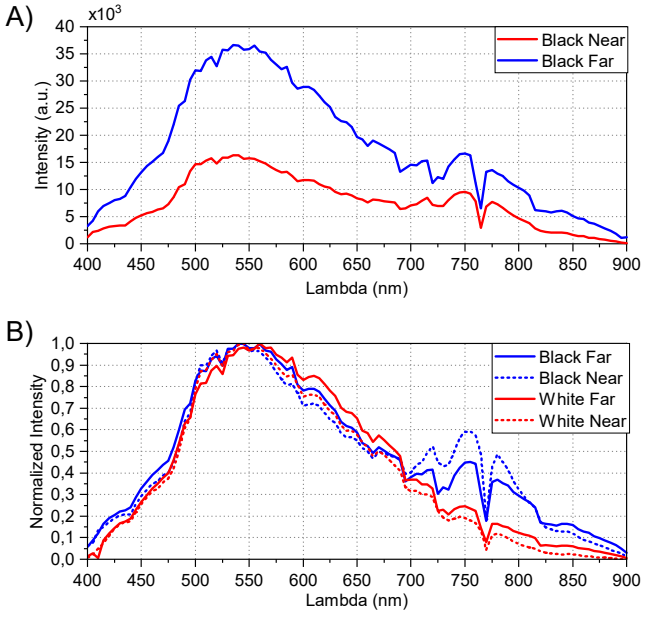

Fig. 7. Intensity spectra (A) and normalized spectra(B) for the two diffuser screens in the VIS region.

pointing the two devices to the black screen. The signal on the Near device, $S^{b}_{Near}(\lambda)$, is simply the small fraction of the sun radiation reflected by the black screen, whereas the measurement from the Far device, $S^{b}_{Far}(\lambda)$, has two contributions: the radiation reflected by the black screen and the diffuse light that exists in the field of view of the device. This diffuse light has two sources, the direct sun radiation and the beams reflected from the heliostat field, so its contribution varies along the day and between days in both intensity and spectrum.

The analysis of the diffuse light due to the heliostat beams is essential for an accurate measurement of the atmospheric attenuation value. As an example, in Fig. 7a we show the VIS measured spectra with the black screen one day at midday on December (integration time 500 ms). The difference between the blue and red curves is the contribution of the diffuse light. This contribution is in the order of 10% of the signals measured with the white screen, shown in Fig. 4.

The spectrum of this diffuse light is different than the spectrum of the radiation reflected on the white screen. This is evident in Fig. 7b, where we show the normalized spectra measured at the same hour using the black and white screens. Therefore, the relative contribution of the diffuse light varies along the spectral range. Nevertheless, this has no impact on our results, as Eq. (1) calculates the attenuation distinctly for each wavelength.

Note that the Far device is located, in our case, close to the receptor, at half the height of the tower. The impact of the background contribution, if not corrected, will become larger the closer this device is to the

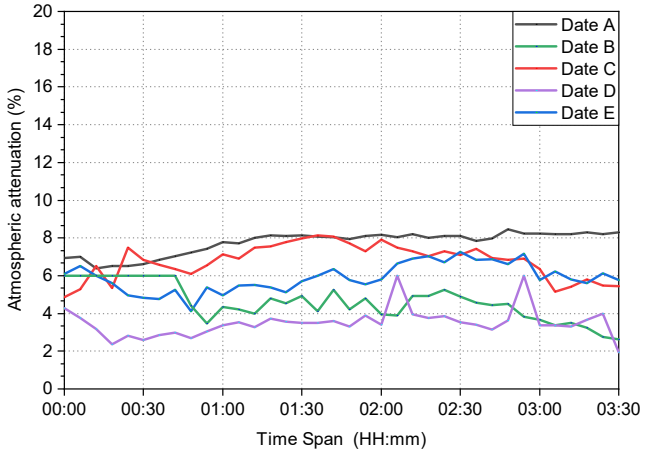

Fig. 8. Atmospheric attenuation for a slant range of 850 m measured for five different days (Date A-D) at the same time span.

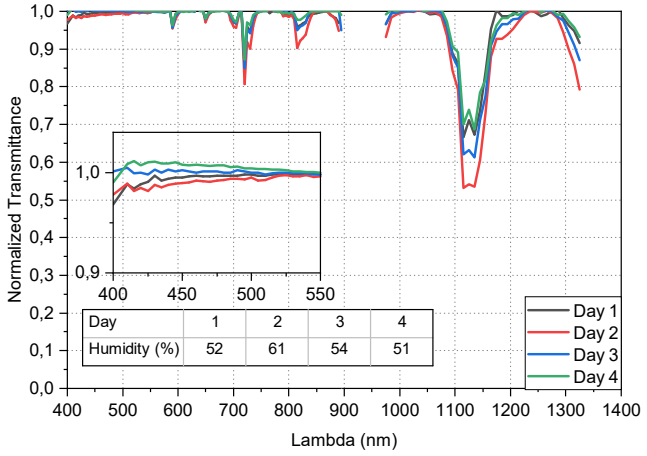

Fig. 9. Normalized transmittance spectrum at the same hour on four different days showing the H_2O absorption peaks at 590 nm, 650 nm, 690–710 nm, 720–730 nm, 820 nm, 1100–1160 nm.

receptor location, as the density of beams from the heliostats increases.

By using the measured parameters $S^{w}_{Far}(\lambda)$, $S^{w}_{Near}(\lambda)$, $S^{b}_{Far}(\lambda)$, $S^{b}_{Near}(\lambda)$ and the previously calibrated $K(\lambda)$, the atmospheric attenuation for the slant path at each wavelength $At_s(\lambda)$ and the solar-weighted atmospheric attenuation At_s are calculated using Eqs. (1) and (2). As an example, we show in Fig. 8 At_s values on 5 different days on December at the same hours. Due to confidentiality, neither hour nor day data are reported.

The results are in the range of those reported in the literature. Measurement campaigns in Southern Spain (Ballestrín et al., 2019) provide similar maximum and minimum monthly values in winter. However, it is important to note that a real comparison would need measurements from different measurement techniques at the same time and location.

Fig. 9 shows the evolution of the measured transmittance spectrum. Data is normalized to a reference measurement taken on December 27, which was the day with the lowest registered relative humidity (44%). This makes it possible to evaluate the changes in the presence on air of different molecules and aerosol particles that cause the attenuation of the reflected light in its way to the receptor and to estimate their impact. The values in the 875 nm-950 nm and over 1300 nm ranges are not presented as they lack precision due to the particular configuration of the equipment (same integration time for any acquisition process).

The variation in the Rayleigh scattering caused by the difference in the presence of aerosol particles can be appreciated in the inlet graph

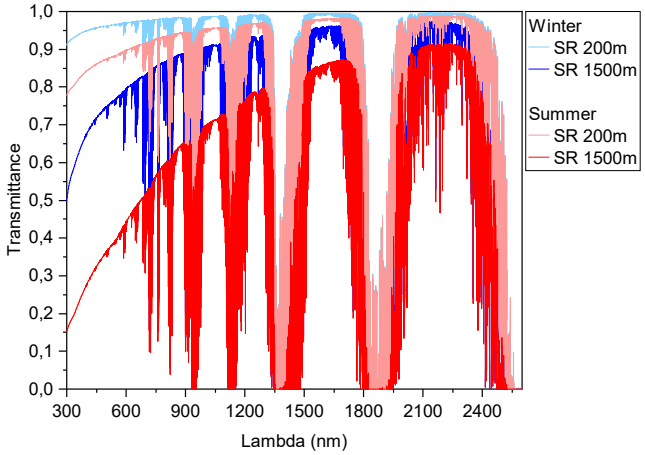

Fig. 10. MODTRAN simulation for two heliostats at different seasons (Winter and Summer) for two different Slant Range (SR 200 m and SR 1500 m).

showing the 400 nm to 550 nm range. The spectral resolved measurement shows also the evolution of the attenuation at the H2O absorption peaks, which are clearly detected at their corresponding wavelengths, over different days on December and January. There is good correlation between the relative humidity data for the same time intervals obtained from the Spanish Meteorological Agency AEMET (also shown on the figure) and the size of these absorption peaks, showing that the concentration of water molecules in air, averaged over the slant range, can be assessed using the spectra obtained from this setup.

The analysis of the different contributions to the attenuation spectrum opens the way to generate accurate models to evaluate the global atmospheric attenuation in a CR-CSP plants (Elias et al., 2021; Franchini et al., 2013; Mishra et al., 2020). This is especially relevant in real scenarios where the spectral and seasonal dependence of the attenuation is large, for example in desert areas.

As an example of this variability, Fig. 10 shows the spectral transmittance of solar radiation reflected by heliostats calculated with MODTRAN 6.0 for a location in the Arabian Desert. There are marked differences in the transmittance as a function of both the slant range (200 m and 1500 m) and season (Summer and Winter), due to the different contributions of scattering and absorption processes by aerosol particles and air molecules.

The transmittance is clearly wavelength dependent, but this dependence varies with the slant range, due to the differences in the contributions of scattering and absorption by aerosol particles and air molecules. The spectral measurement allows to independently quantify these contributions and, from this knowledge, to incorporate accurate data into the proper model to calculate the atmospheric attenuation for any heliostat of the plant. Finally, from the estimation of the attenuation for each of the heliostats of the CR-CSP plant, it can also be calculated the global solar energy reaching the receptor.

4. Conclusion

A new measurement strategy and system for the measurement of atmospheric attenuation in solar plants is presented. It is based on the measurement, at two different locations on the plant, of the VIS and IR spectra of the sun radiation reflected by a white diffuser screen. This system uses optical telescopes to make possible spectral measurements with the wavelength resolution and intensity precision required.

With the spectral information acquired, we can calculate both the atmospheric attenuation at each wavelength in the solar optical range and the solar-weighted attenuation, without inaccuracies due to wavelength dependencies of the different contributions to the measurement, such as the atmospheric attenuation sources or the diffuse light

background existing in the plant. Moreover, this data allows us to study the different origins of the atmospheric attenuation with enough wavelength resolution to identify molecular absorption bands – such as those of the water - or the wavelength dependence of the scattering from aerosol particles. The identification and quantification of these contributions opens the way to generate accurate models to calculate the atmospheric attenuation of the radiation reflected by any heliostat of the solar plant, including the dependence of the attenuation spectrum with the distance. And, by integrating the attenuation for all the heliostats of the solar plant, the global solar energy reaching the receptor can be calculated.

The system has been set up and tested at PS10, a commercial solar thermal power plant, with central receiver system at Sanlúcar la Mayor (Seville, Spain) owned by Atlantica Sustainable Infrastructure Plc. The experimental results validate the measurement strategy and show its advantages over previous methods.

Declaration of Competing Interest

The authors declare that they have no known competing financial interests or personal relationships that could have appeared to influence the work reported in this paper.

Acknowledgment

The authors would like to thank Atlantica staff at Sanlúcar la Mayor for their assistance with the installation and maintenance of the measurement setup, and for providing all the necessary means for the completion of our field work.

Funding

This research did not receive any specific grant from funding agencies in the public, commercial, or not-for-profit sectors.

References

Ali Rahoma, U., Hassan, A.H., 2012. Determination of atmospheric turbidity and its correlation with climatologically parameters. Am. J. Environ. Sci. 8, 597–604. https://doi.org/10.3844/ajessp.2012.597.604.

Ballestrín, J., Carra, E., Monterreal, R., Enrique, R., Polo, J., Fernández-Reche, J., Barbero, J., Marzo, A., Alonso-Montesinos, J., López, G., Batlles, F.J., 2019. One year of solar extinction measurements at Plataforma Solar de Almería. Application to solar tower plants. Renew. Energy 136, 1002–1011. https://doi.org/10.1016/j.renene.2019.01.064.

Ballestrín, J., Marzo, A., 2012. Solar radiation attenuation in solar tower plants. Sol. Energy 86 (1), 388–392. https://doi.org/10.1016/j.solener.2011.10.010.

Ballestrín, J., Monterreal, R., Carra, M.E., Fernández-Reche, J., Polo, J., Enrique, R., Rodríguez, J., Casanova, M., Barbero, F.J., Alonso-Montesinos, J., López, G., Bosch, J.L., Batlles, F.J., Marzo, A., 2018. Solar extinction measurement system based on digital cameras. Application to solar tower plants. Renew. Energy 125, 648–654. https://doi.org/10.1016/j.renene.2018.03.004.

Brady, D.J., 2008. Optical Imaging and Spectroscopy, Optical Imaging and Spectroscopy. John Wiley and Sons. https://doi.org/10.1002/9780470443736.

D'Amato, D.P., Griffiths, D., Leland, J.E., 2007. Linearity improvement in a high dark-current short-wave infrared array spectrometer, in: Earth Observing Systems XII. SPIE, p. 66770C. https://doi.org/10.1117/12.732568.

Elias, T., Ramon, D., Dubus, L., Am-Shallem, M., Kroyzer, G., 2021. DNI and slant path transmittance for the solar resource of tower thermal solar plants: The validation of the ASoRA method and impact in exploiting a global data set. Sol. Energy 217, 78–92. https://doi.org/10.1016/j.solener.2020.12.064.

Fernández-Peruchena, C.M., Vignola, F., Gastón, M., Lara-Fanego, V., Ramírez, L., Zarzalejo, L., Silva, M., Pavón, M., Moreno, S., Bermejo, D., Pulgar, J., Macias, S., Valenzuela, R.X., 2018. Probabilistic assessment of concentrated solar power plants yield: The EVA methodology. Renew. Sustain. Energy Rev. 91, 802–811. https://doi.org/10.1016/j.rser.2018.03.018.

Franchini, G., Perdichizzi, A., Ravelli, S., Barigozzi, G., 2013. A comparative study between parabolic trough and solar tower technologies in Solar Rankine Cycle and Integrated Solar Combined Cycle plants. Sol. Energy 98, 302–314. https://doi.org/10.1016/j.solener.2013.09.033.

Hanrieder, N., Sengupta, M., Xie, Y., Wilbert, S., Pitz-Paal, R., 2016. Modeling beam attenuation in solar tower plants using common DNI measurements. Sol. Energy 129, 244–255. https://doi.org/10.1016/j.solener.2016.01.051.

Hanrieder, N., Wilbert, S., Mancera-Guevara, D., Buck, R., Giuliano, S., Pitz-Paal, R., 2017. Atmospheric extinction in solar tower plants – A review. Sol. Energy. 152, 193–207. https://doi.org/10.1016/j.solener.2017.01.013.

Ineichen, P., 2008. Conversion function between the Linke turbidity and the atmospheric water vapor and aerosol content. Sol. Energy 82 (11), 1095–1097. https://doi.org/10.1016/j.solener.2008.04.010.

Marzo, A., Salmon, A., Polo, J., Ballestrín, J., Soto, G., Quiñones, G., Alonso-Montesinos, J., Carra, E., Ibarra, M., Cardemil, J., Fuentealba, E., Escobar, R., 2021. Solar extinction map in Chile for applications in solar power tower plants, comparison with other places from sunbelt and impact on LCOE. Renew. Energy 170, 197–211. https://doi.org/10.1016/j.renene.2021.01.126.

Mishra, B.R., Hanrieder, N., Modi, A., Kedare, S.B., 2020. Comparison of three models to estimate the slant path atmospheric attenuation in central receiver solar thermal plants under Indian climatic conditions. Sol. Energy 211, 1042–1052. https://doi.org/10.1016/j.solener.2020.10.049.

Molineaux, B., Ineichen, P., 1996. On the broad band transmittance of direct irradiance in a cloudless sky and its application to the parameterization of atmospheric turbidity. Sol. Energy 56 (6), 553–563. https://doi.org/10.1016/0038-092X(96)00016-3.

Polo, J., Ballestrín, J., Carra, E., 2016. Sensitivity study for modelling atmospheric attenuation of solar radiation with radiative transfer models and the impact in solar tower plant production. Sol. Energy 134, 219–227. https://doi.org/10.1016/j.solener.2016.04.050.

Sánchez, M., Fernández-Peruchena, C.M., Bernardos, A., Heras, C., Chueca, R., Salinas, I., 2019. High-accuracy real-time monitoring of solar radiation attenuation in commercial solar towers. In: AIP Conference Proceedings. American Institute of Physics Inc., p. 30021. https://doi.org/10.1063/1.5117561

Schroeder, D., 2000. Astronomical Optics, 2nd Editio. ed, Astronomical Optics. Elsevier. https://doi.org/10.1016/b978-0-12-629810-9.x5000-2.

Shaw, G.E., Reagan, J.A., Herman, B.M., 1973. Investigations of Atmospheric Extinction Using Direct Solar Radiation Measurements Made with a Multiple Wavelength Radiometer [WWW Document]. J. Appl. Meteorol. https://doi.org/10.1175/1520-0450(1973)012<0374:ioaeud>2.0.co;2.

Smith, W.J., 2007. Modern Optical Engineering, 4th Edition. ed. McGraw-Hill Education. https://doi.org/10.1036/0071476873.

Solnova Solar Power Plant [WWW Document], n.d. URL https://www.atlantica.com/web/en/company-overview/our-assets/asset/solnova-1-3-4/ (accessed 6.16.21).

Tahboub, Z.M., Obaidli, A.A.A., Luque, F., Salbidegoitia, I., Farges, O., Hassar, Z., Oumbe, A., Geuder, N., Goebel, O., 2012. Solar Beam Attenuation Experiments – Abu Dhabi, in. SolarPACES Conference.

Wen, C.-C., Yeh, H.-H., 2010. Comparative influences of airborne pollutants and meteorological parameters on atmospheric visibility and turbidity. Atmos. Res. 96 (4), 496–509. https://doi.org/10.1016/j.atmosres.2009.12.005.